JOURNAL OF MATERIALS SCIENCE 30 (1995) 2921–2929

Transformation of the quasicrystalline phase Al–Cr–Fe induced by rapid solidification

A. ZIANI, G. MICHOT, A. PIANELLI*, A. REDJAÏMIA‡
*Ecole des Mines de Nancy, Parc de Saurupt, 54042 Nancy Cedex, France, URA C.N.R.S.155, *159,‡1402*

C. Y. ZAHRA, A. M. ZAHRA
Centre de Thermodynamique et Microcalorimétrie, 26 rue du 141e R.I.A., 13003 Marseille, France, UPR C.N.R.S. 7461

A quasicrystalline phase, Q, with icosahedral symmetry was detected by X-ray diffraction and transmission electron microscopy in Al–3Cr–*x*Fe ($x=0$, 1 or 3 at %) alloys elaborated by hot extrusion of rapidly solidified powders. Chemical microanalysis showed the average composition of this phase to be $75\pm0.5\%$ Al, $12\pm1\%$Cr, $12\pm1\%$ Fe. Annealing treatments led to its transformation into the equilibrium phases $Al_{13}Cr_2$ and $Al_{13}Fe_4$, directly at high temperature, or through a metastable and unknown phase, X, at intermediate temperature. This transformation was followed by X-ray diffraction, calorimetry and *in situ* electron microscopy. The convergent-beam technique was used for characterization of the X phase.

1. Introduction

The substantial increase in solid solubility achieved by rapid solidification offers the prospect of developing new alloy compositions, with improved thermal stability based on addition elements with low equilibrium solubilities and mobilities in solid aluminium. Among the most possible alloy systems are those based on the aluminium-transition metal systems and especially Al–Fe–X [1, 2] and Al–Cr–X [3, 4] produced by several different atomization techniques. Recently, promising values of elongation and fracture toughness have been reported [5] for an Al–4Cr–1Fe mass %. In these alloys, rapid solidification produces cellular/dendritic or microeutectic solidification structures with equilibrium and quasicrystalline phases that decompose during subsequent thermomechanical processing.

2. Experimental procedure

The alloys were prepared from pure aluminium and the master alloys Al–6.0 at % Cr and Al–15.4 at % Fe, molten at 1200 °C in an induction furnace under an argon atmosphere. The rapid solidification was achieved by centrifugal atomization: the alloy heated at 1200 °C falls on to a disc spun at a rate of 27 000 r.p.m.: the liquid spreads and divides on the disc edge into droplets which solidify during their flight in the helium atmosphere. The powder lot 50–100 μm in diameter is canned and degassed at 330 °C for 3 h. Then the can is closed when the powder is again at room temperature and the pressure over it lower than 10^{-5} Pa.

The can was preheated at 340 °C before extrusion through a conical die, with a semi-angle equal to 45° (extrusion ratio of 25:1). The chemical compositions of the ternary consolidated alloys, as determined by atomic absorption, were Al–3.11Cr–1.06Fe and Al–2.92Cr–3.12Fe (at %). The powders and the consolidated alloys were examined by X-ray diffraction (XRD) using CoK_α radiation, scanning and transmission electron microscopy (SEM, TEM). Chemical microanalysis on consolidated alloys was performed in a scanning transmission electron microscope (STEM): quantification of the X-ray information was accomplished by using the Cliff–Lorimer method [6], when the condition of thin-film approximation was fulfilled. The transformation of the quasicrystalline phase was followed by isothermal and differential scanning calorimetry (DSC) for the consolidated material. The convergent-beam technique was used for characterizing the metastable X phase.

3. Results and discussion

3.1. X-ray diffraction measurements

Two isothermal sections, at 425 and 600 °C, of the Al–Cr–Fe equilibrium phase diagram have already been experimentally determined in the aluminium-rich corner [7]: no ternary compound appears at these temperatures in equilibrium with the α-aluminium-rich solution, only the three-phase triangle [$\alpha + Al_{13}Cr_2 + Al_{13}Fe_4$] exists. Besides these stable phases, two metastable ones have been reported after rapid solidification: the intermetallic compound Al_6Fe and the icosahedral phase Al–Cr–Fe. XRD studies of the latter [8–11] show that the measured interplanar distances decrease with the value of the ratio Cr:Fe. The diffraction peaks of the Q phase in the alloy Al–5Cr–4Fe (at %) [8] were used for the detection of

0022–2461

our icosahedral phase: the approximation is $\sim 0.5\%$. The double Bragg angle explored ranges from 15°–150°.

Sound examinations need a comparison between the intensity ratios of the diffracted peak versus the (1 1 1) α-Al peak. Difficulties arose from peaks overlapping. For instance, the (8 2 0) peak of $Al_{13}Cr_2$ ($d = 0.20665$ nm) [12] is very close to the (1 1 0 0 0 0) peak due to the icosahedral phase ($d = 0.206$ nm) [8]. The peaks (3 1 0) and (0 2 5) diffracted by Al_6Fe [13, 14] ($d = 0.20613$ nm) and $Al_{13}Fe_4$ [14, 15] ($d = 0.2049$ nm) overlap likewise.

In the as-solidified powder particles of the alloy Al–3Cr, X-ray examination indicated that apart from the α-Al, only the equilibrium $Al_{13}Cr_2$ was formed. The same phases were detected again in the as-extruded alloy. Although no icosahedral phase was detected by XRD, some spherical quasicrystals with icosahedral point group symmetry were observed exceptionally by TEM. Such a discrepancy is not unusual: the spherical icosahedral phase shown by TEM imaging [16] in an Al–4 at %Cr was not detected by XRD. The present phases are extremely fine and the volume fraction of the quasicrystalline phase is too low to give peaks coming out from the background signal. Thus, in the following sections only the Al–3Cr–1Fe and Al–3Cr–3Fe alloys will be considered. The results of the phase identification on the consolidated material are given in Table I.

3.2. Microstructures of the as-consolidated material

Longitudinal sections of Al–3Cr–1Fe, as observed by SEM and TEM are presented, respectively, in Fig. 1a and b. The observed band structure results from

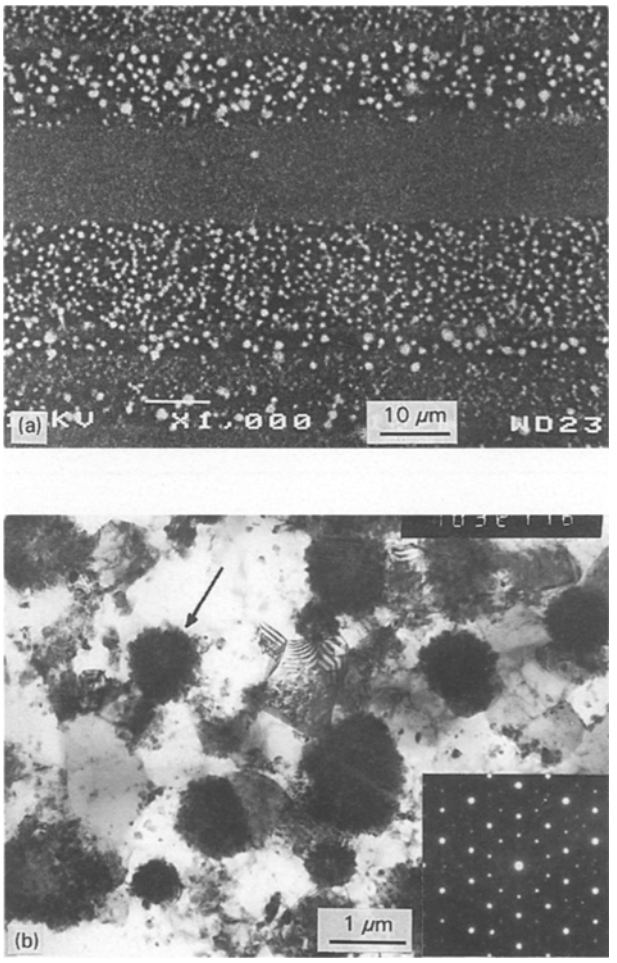

Figure 1 Longitudinal section of the extruded bar (Al–3Cr–1Fe alloy): (a) band structure (SEM), (b) SAD pattern of the quasicrystal marked by an arrow on the bright-field image (TEM).

TABLE I The results of the phase identification on the consolidated material

	Icosa. phase		$Al_{13}Cr_2$		Al_6Fe		$Al_{13}Fe_4$	
	N	$I_{1\,1\,0\,0\,0\,0}$	N	$I_{8\,2\,0}$	N	$I_{1\,3\,1}$	N	$I_{2\,0\,5}$
Al–3Cr–1Fe								
As-consolidated alloy	Very weak + overlapping		7	7	Very weak + overlapping		Not detected	
Exposed at 300 °C/256 h	Very weak + overlapping		7	8	Weak + overlapping		Very weak + overlapping	
Exposed at 500° C/256 h	Not detected		7	8	Weak + overlapping		Weak + overlapping	
Al–3Cr–3Fe								
As-consolidated alloy	7	13	Not detected		Not detected		Not detected	
Exposed at 300 °C/256 h	7	14	Not detected		Not detected		Not detected	
Exposed at 333 °C/256 h	Weak + overlapping		8	16[a]	5	7	Not detected	
Exposed at 367 °C/256 h	Very weak + overlapping		8	16[a]	6	8	Not detected	
Exposed at 400 °C/256 h	Not detected		8	16[a]	6	7	Not detected	
Exposed at 500 °C/256 h	Not detected		8	11	Not detected		7	8

$I_{h\,k\,l}$ is defined as the ratio (%) of the ($h\,k\,l$) peak height over the (1 1 1) peak height of the α-Al matrix. N is the number of observed diffraction peaks.

[a]The relatively high intensity is due to an overlapping.

microstructural inhomogeneities in powders, i.e. differences in volume fractions of precipitates, mainly $Al_{13}Cr_2$ and Q phases. In addition to a much better microstructural homogeneity, equivalent results are obtained on the Al–3Cr–3Fe alloy: such a homogeneous distribution is connected to a more definite phase stoichiometry as checked by EDX measurements performed on an STEM. The following average composition for the Q phase was obtained: (75 ± 0.5)Al, (12 ± 1)Cr and (12 ± 1)Fe (at %). In the following sections only the nearly homogeneous alloy, i.e. Al–3Cr–3Fe, will be considered.

3.3. Transformation products of the Q-phase

3.3.1. "Low"-temperature behaviour

No difference in the XRD pattern was detected between the as-consolidated alloys and that annealed for 256 h at 300 °C. Conversely, exposure at 333 °C for the same time leads to a decrease in the volume fraction of the Q phase (peaks 2 and 5 of Fig. 2) to the benefit of the Al_6Fe phase (peak 1) and $Al_{13}Cr_2$ equilibrium phase (peaks 4 and 6). TEM observations of the alloy after annealing at 400 °C for 256 h confirm the presence of the $Al_{13}Cr_2$ and Al_6Fe phases but, in addition, a bulky unknown phase, called X, was frequently detected (Fig. 3).

This phase evolution, occurring between 300 and 400 °C, will be referred to as a low-temperature phase transformation, in contrast to the high-temperature transformation, which will be described below.

3.3.2. "High" temperature behaviour

XRD patterns achieved on samples exposed 256 h at 400 or 500 °C are presented in Fig. 4. Between the (1 1 1) and (2 0 0) intense peaks of α-Al, eleven peaks are noticed. Table II summarizes the possible corresponding phases. It seems quite clear that at 500 °C only the stable phases remain: as underlined by the disappearance of peak 1, the metastable Al_6Fe has vanished while the equilibrium $Al_{13}Fe_4$ phase is

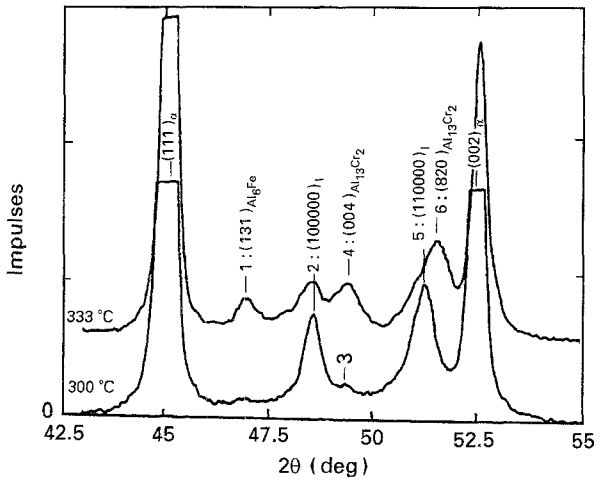

Figure 2 XRD patterns of consolidated Al–3Cr–3Fe alloy after exposure at 300 or 333 °C for 256 h.

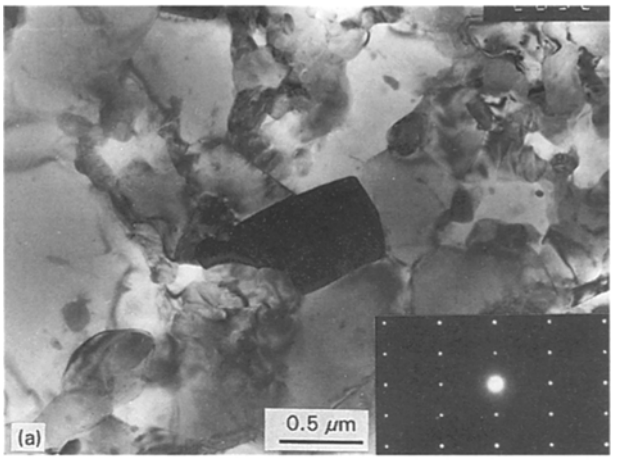

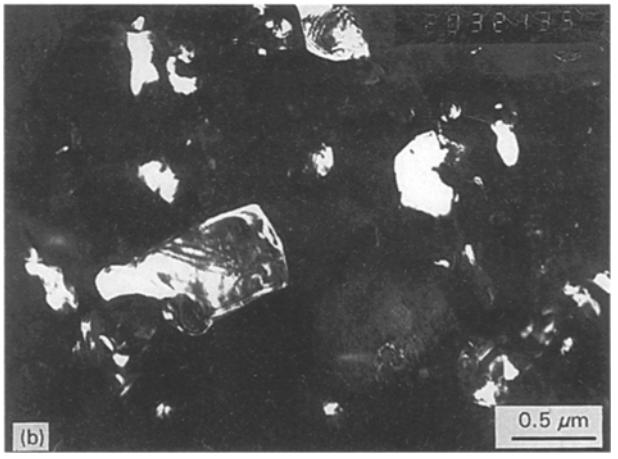

Figure 3 TEM observations of the metastable X phase precipitated in Al–3Cr–3Fe alloy after exposure at 400 °C for 256 h: (a) bright-field and selected-area diffraction (SAD) pattern (b) dark-field.

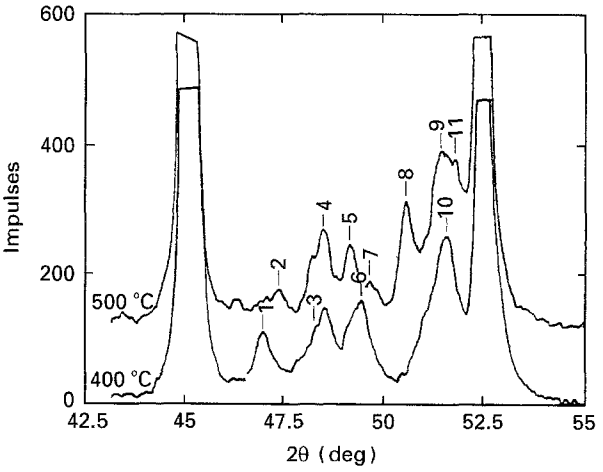

Figure 4 XRD patterns of consolidated Al–3Cr–3Fe alloy after exposure at 400 or 500 °C for 256 h.

reinforced (peak 8). However, the indexation of peaks 9–11 requires some comment. Rapid quenching, as well as easy substitution of chromium by iron on the network of the $Al_{13}Cr_2$ phase, lead to large variations in the compound stoichiometry. For this reason, the two most intense peaks (9 and 11, Table II) fully overlap, giving broad peaks at low temperature (peaks 6 of

TABLE II Proposed phase identification for XRD patterns of Fig. 4

Peak number	Interplanar	distances	Proposed phases	Interplanar distances	Diffraction peaks
1	0.2246	–	Al_6Fe	0.2243	(1 3 1)
2	–	0.2228	$Al_{13}Cr_2$	0.2229	($\bar{5}$ 3 2)
3	0.2188	0.2192	Al_6Fe	0.2194	(0 0 4)
			$Al_{13}Cr_2$	0.2197	($\bar{1}\,\bar{1}$ 1 3)
4	0.2178	0.2179	$Al_{13}Cr_2$	0.2182	($\bar{8}$ 0 5)
5	0.2153	0.2151	$Al_{13}Cr_2$	0.2153	(3 3 1)
6	0.2142	–	X?	?	?
7	–	0.2131	$Al_{13}Cr_2$	0.2138	(0 0 4)
8	–	0.2095	$Al_{13}Fe_4$	0.2095	($\bar{6}$ 2 3) and (2 0 5)
9	–	0.2061	$Al_{13}Cr_2$	0.2067	8 2 0
10	0.2057	0.2055	$Al_{13}Cr_2$	Broad peak = (8 2 0)	+ ($\bar{5}$ 1 5)
11	–	0.2048	$Al_{13}Cr_2$	0.2049	($\bar{5}$ 1 5)
			$Al_{13}Fe_4$	0.2049	(0 2 5) and ($\bar{6}$ 0 5)

Fig. 2 and 10 of Fig. 4), while easier diffusion at high temperature improves the crystalline quality and thermodynamical stability of this phase, leading to a splitting (peaks 9 and 11 of Fig. 4). Because peak 6 (Fig. 4) cannot be related to a known phase, the X phase may be invoked.

SEM and TEM observations after 256 h at 500 °C reveal large needle-like precipitates of $Al_{13}Fe_4$, about 7–15 μm in length as confirmed by SAD (Fig. 5).

In addition to this information on the transformation products, some kinetic informations can be derived from *in situ* heating and observation in the single-tilt hot stage of the transmission electron microscope or from calorimetric studies.

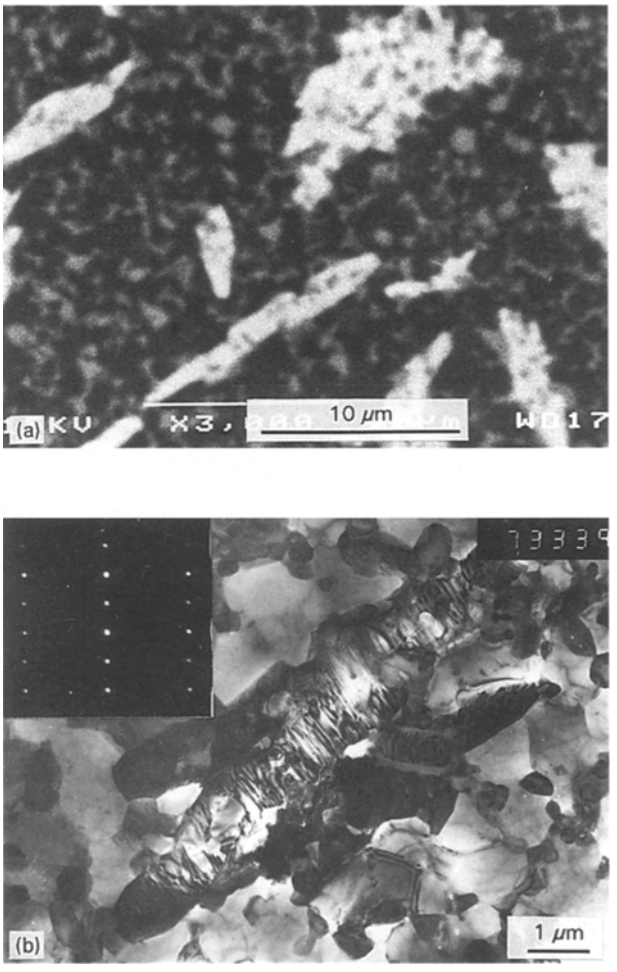

Figure 5 (a) Scanning electron and (b) transmission electron micrographs showing needle-like precipitates of $Al_{13}Fe_4$ in Al–3Cr–3Fe alloy after 256 h at 500 °C. The SAD pattern (b) corresponds to a [0 1 0] zone axis.

3.4. *In situ* observations

The initial microstructure (Fig. 6a) is characterized by quasicrystals embedded into the α-Al matrix. Rapid heating to 400 °C after exposure for 15 min at 350 °C does not produce any change in the small quasicrystal marked by the letter Q in the micrographs 6a and 6b. After exposure for 60 min at 400 °C (Fig. 6c), and holding at 450 °C for 15 min (Fig. 6d), the appearance and growth of an elongated precipitate (marked by an arrow) is noticed at the quasicrystal/matrix interface, while the quasicrystal size decreases. The corresponding SAD pattern (fine network of Fig. 6e) shows the same characteristics and symmetry as those of the metastable phase X previously mentioned (Fig. 3).

As expected from the difference in driving force for transformation linked to curvature radius, the larger the quasicrystal size the lower the transformation rate: the large quasicrystal shown in Fig. 7a and b is still unchanged after the thermal treatments reported in the previous paragraph. However, a significant change in morphology occurs during the subsequent exposures at 500 °C for 12 min (Fig. 7c) or 15 min (Fig. 7d). The precipitated phase (marked by an arrow in Fig. 7d) is the equilibrium $Al_{13}Fe_4$ phase, as checked by the SAD pattern of (Fig. 7e).

3.5. Calorimetric measurements

A strong exothermic peak of the order of $-20\ J\ g^{-1}$ which goes beyond 530 °C (the actual limit of our apparatus) is observed on the DSC curve of Fig. 8. For a lower scan rate (1 instead of 10 $K\ min^{-1}$), a secondary weak peak is detected at high temperature (Fig. 9). The activation energy for the main transformation, as derived from DSC scans made at five different rates according to the Kissinger method [17], equals $193 \pm 5\ kJ\ mol^{-1}$. This value is very close to that for iron diffusion in aluminium (193 [18] or 183 $kJ\ mol^{-1}$

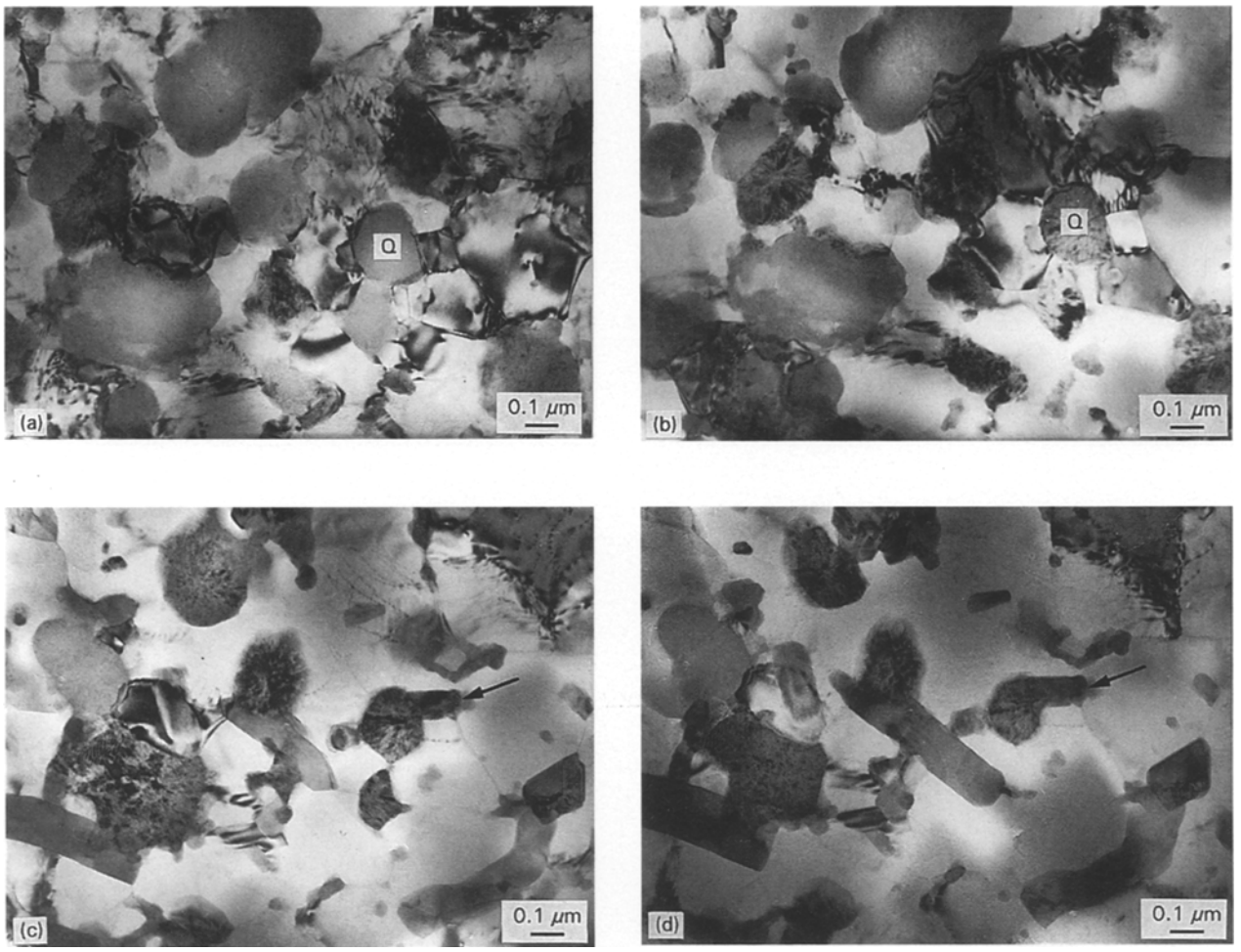

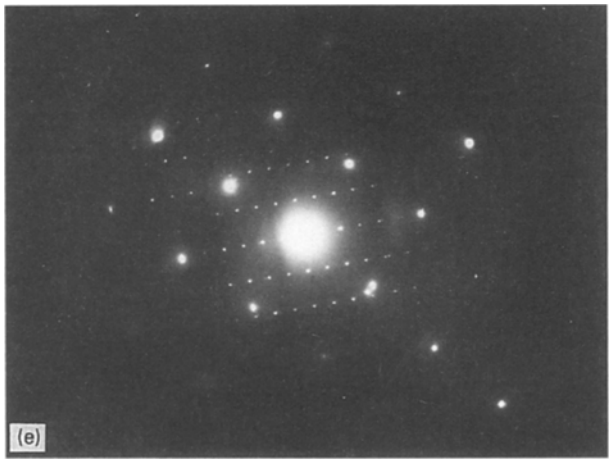

Figure 6 *In situ* observations of the different transformation steps of the quasicrystalline phase (see text for details).

[19]) and quite different from chromium diffusion (260 kJ mol^{-1} [20]) or self diffusion (120 kJ mol^{-1}) [21]). Hence the overall transformation is controlled by iron diffusion.

Under isothermal conditions ($T = 333\,^{\circ}C$) it appears from a decomposition of the observed heat fluxes that a fast exothermic effect vanishing over 50 h (curve (a), Fig. 10) is superimposed upon a slower one (curve (b) Fig. 10) which passes by a minimum characteristic of a nucleation and growth process. The enthalpy released between 10 and 360 h as measured on the slow transformation, compares quite well with that measured under the DSC main peak, considering that 1 mole corresponds to 28.6 g.

In such rapidly solidified alloys, the appearance of new phases can be related to the transformation of the supersaturated solid solution α-Al or/and to that of the Q phase. X-ray diffraction shows that the change in α-Al parameter induced by the supersaturation and detected in the powder, is no longer observed in the consolidated material. Thus, even if local supersaturations are sometimes detected by EDX we may neglect the precipitation linked to the α-Al with respect to the Q phase crystallization products. It may be assumed from the calorimetric studies that the slow Q phase transformation proceeds via a nucleation -and-growth mechanism involving a long-range transport of iron atoms. According to XRD, the metastable Al_6Fe phase appears at temperatures between 333 and 400 °C. *In situ* TEM experiments show that nucleation of either the X phase (Fig. 6) or the $Al_{13}Fe_4$ phase (Fig. 7) occurs at the Q/α-Al interface; there growth also implies iron diffusion through the matrix because both phases are based on the binary Al–Fe system (see Section 3.6 for X phase composition). The transformation of binary Al–Cr or Al–Fe quasicrystals is accompanied by an activation energy of only 140 kJ mol^{-1} [10]; this value is closer to that for self diffusion than to that for iron or chromium diffusion: the required structural rearrangements are probably facilitated by the presence of excess vacancies.

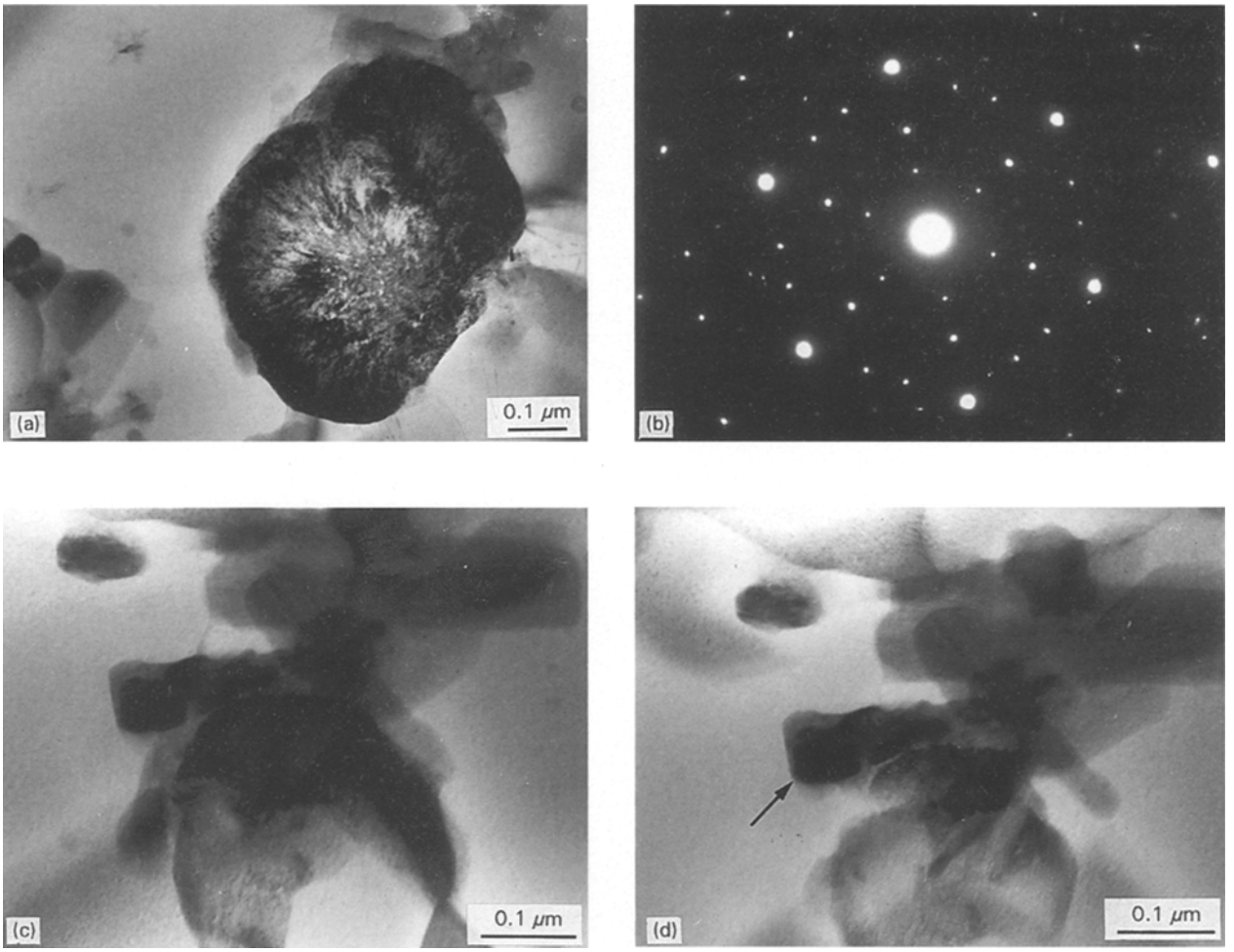

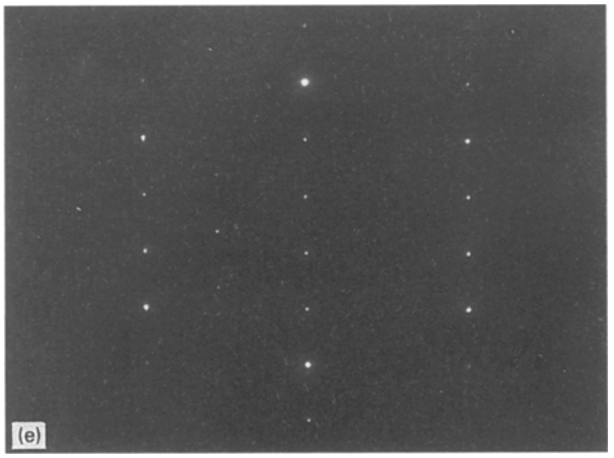

Figure 7 *In situ* observation of high-temperature transformation of large quasicrystals. The SAD pattern (e) corresponds to the [0 1 0] zone axis of the $Al_{13}Fe_4$ phase (see text for details).

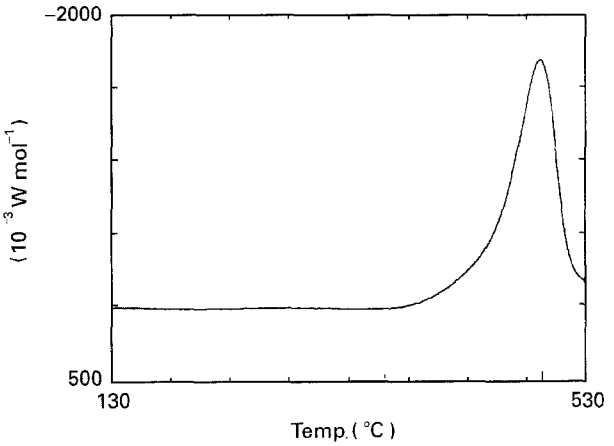

Figure 8 DSC curve of an Al–3Cr–3Fe (at %) alloy. Heating rate 10 K min^{-1}.

The fast kinetic process, as given by Fig. 10 (curve a), may be linked to some $Al_{13}Cr_2$ precipitation at interfaces and/or to the restoration of the residual deformation microstructure after extrusion.

It is noteworthy that a secondary peak, such as that shown in Fig. 9, is also noticed during transformation of Al–Cr [23] or Al–Mn [24] quasicrystals. In both cases it is attributed to an intermediate phase between the quasicrystal and the equilibrium phase: it is then tempting to relate our peak to the metastable X phase. Alternatively, it may correspond to the transition of the metastable Fe_6Al and X phases into the stable $Al_{13}Fe_4$ phase.

3.6. Characterization of the X phase

Because all the attempts to link the SAD patterns to the known Al–Cr and Al–Fe phases failed, other techniques were applied. Two- and three-dimensional symmetry information required for the crystallographic structure determination of an unknown phase, present as small particles dispersed in a matrix,

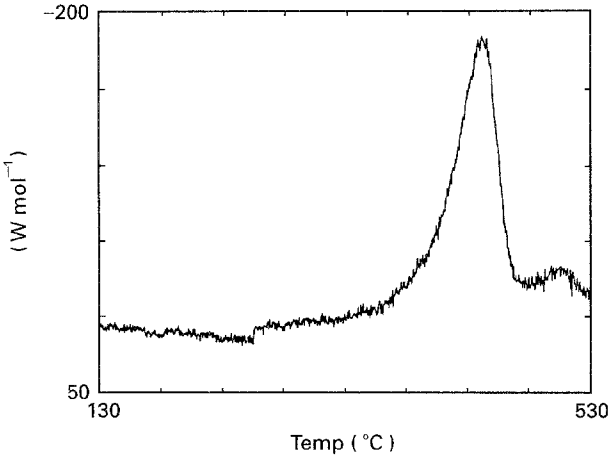

Figure 9 DSC curve of an Al–3Cr–3Fe (at %) alloy. Heating rate 1 K min^{-1}.

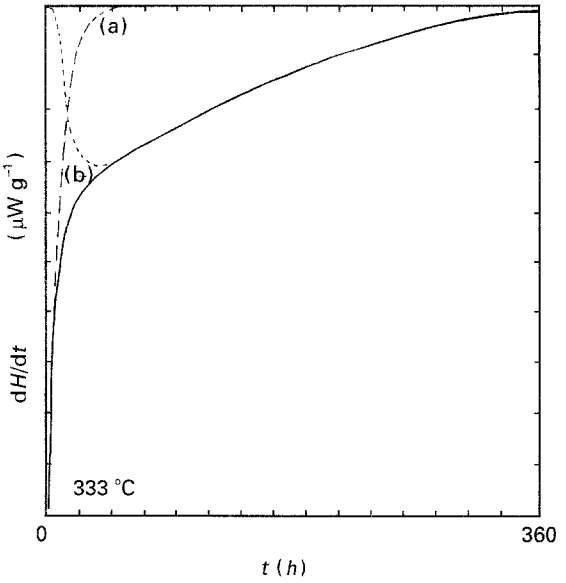

Figure 10 Isothermal microcalorimetry: heat flux versus time at 333 °C. The resulting signal is decomposed into a fast mechanism (curve a) and a slow one (curve b).

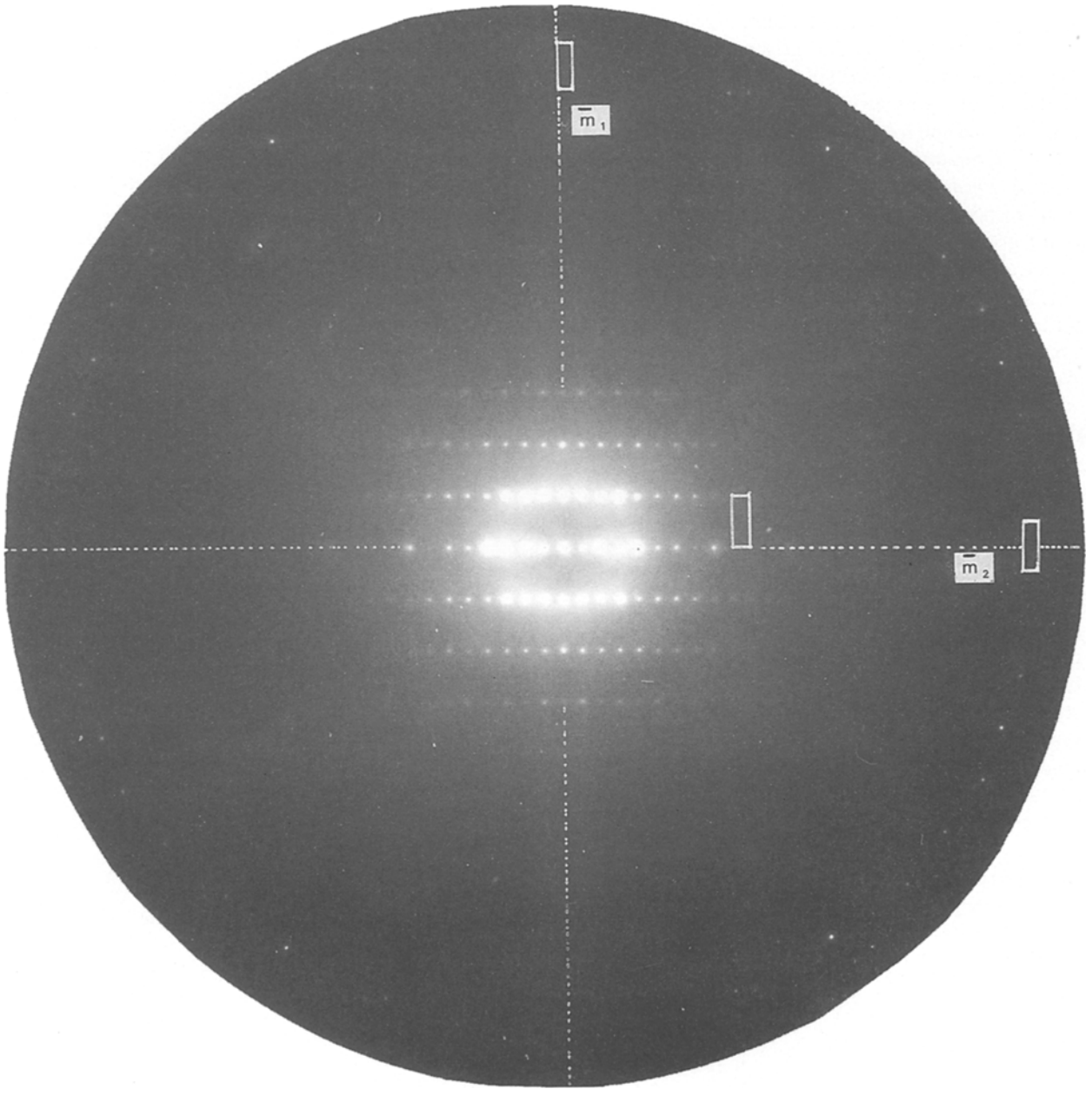

Figure 11 [001] ZAP of the X phase. Two perpendicular mirrors, $\overline{m}_1$ and $\overline{m}_2$, indicate a 2 *mm* symmetry.

cannot generally be deduced directly from convergent-beam electron diffraction patterns (CBED). This is better achieved through microdiffraction patterns obtained by focusing a nearly parallel beam on to a very small area. The zone-axis microdiffraction patterns (ZAPs), thus obtained, are composed of small diameter discs grouped into ZOLZ and HOLZ (zero- and high-order Laue zones). From the "net" and "ideal" symmetries of these patterns, and the shift and periodicity differences between the ZOLZ and HOLZ, it is possible to determine the crystallographic features of the phase [25].

Among the investigated ZAPs of the X phase, it appears that the highest whole pattern net symmetry corresponds to 2 mm (Fig. 11). According to [25], the phase has an orthorhombic structure. For that system, the ZAPs needed for the identification of the Bravais lattice and the glide planes are [1 0 0], [0 1 0] and [0 0 1]. Examination of the latter and its comparison with the theoretical one established elsewhere [25] reveal that the extinction symbol is A--- (in that convention, $c < a < b$): the corresponding possibilities for space and point groups are summarized in Table III.

The number of possible groups can be restricted through the identification of the point group by means of the "ideal" symmetries which take into account the position and the intensities of the diffracted discs. The "ideal" symmetries from the [0 0 1] ZAP (Fig. 11) are ($2\,mm$) $2\,mm$ from the ZOLZ and the whole pattern, respectively. According to Morniroli [25] the point group is either $mm2$ or mmm. To remove the uncertainty, an examination of [1 0 0] and [0 1 0] ZAPs is required: unfortunately, the quality of such patterns is not good enough to reveal the "ideal" symmetry. Finally, the space group is either $A2mm$, $Amm2$($Am2m$) or $A\frac{2}{m}A\frac{2}{m}A\frac{2}{m}$.

From the [0 0 1] ZAP (Fig. 11) it is possible to deduce the following lattice parameters: $a = 0.64$ nm, $b = 0.84$ nm and $c = 0.62$ nm.

Based on EDX analysis giving a ratio [Al]/[Cr + Fe] equal to 3.1 ± 0.1 it is tempting to attribute to the X phase the following stoichiometry, $Al_3(Fe_{1-x}Cr_x)$, x being much smaller than one, as only a few chromium atoms substitute iron in the Al_3Fe phase. According to our results, this latter phase should be orthorhombic as originally believed, but more recent experiments conclude to a monoclinic structure [26], claiming that the finding of a more symmetrical orthorhombic lattice is due to the strong tendency of the compound to twinning [27]. Twinning, as observed on $Al_{13}Fe_4$ precipitates (see Fig. 5b), is not obvious on the X phase. Thus we should admit that different allotropic variants can be found.

TABLE III Possible space and point groups of the X phase

Extinction symbol	Points groups	Space groups	
A---	222	$A2_122$	(20)
		A222	(21)
	$mm2$	$A2mm$	(35)
		$Amm2$ or	
		$Am2m$	(38)
	mmm	$A\frac{2}{m}\frac{2}{m}\frac{2}{m}$	(65)

4. Conclusions

Depending on the temperature range, different phase transformation routes can be followed for a given exposure time (256 h). During the "low"-temperature sequence the icosahedral phase, Q, reacts with the matrix α-Al giving rise to two metastable phases, in addition to the equilibrium $Al_{13}Cr_2$ phase

$$\alpha\text{-Al} + (Q) \rightarrow \alpha\text{-Al} + Al_{13}Cr_2 + Al_6Fe + Al_3Fe$$

Of course, this is an oversimplified view because all these intermetallics can dissolve small amounts of a third element ($Al_{13}[Cr_yFe_{1-y}]_2$ or $Al_3Fe_xCr_{1-x}$ for the X phase...). For kinetic reasons, the precipitation of the equilibrium product $Al_{13}Fe_4$ does not take place. However, at higher temperature (450–550 °C) the quasicrystal transforms directly into the stable phases, by-passing the step of metastable phase formation (unless this latter is too fast to be detected)

$$\alpha\text{-Al} + (Q) \rightarrow \alpha\text{-Al} + Al_{13}Cr_2 + Al_{13}Fe_4$$

Acknowledgements

The authors thank the Commission of the European Communities who supported this work in the EURAM program.

References

1. Y. W. KIM, in "Proceedings of the TMS Symposium, Dispersion Strengthened Aluminium Alloys", edited by Y. W. Kim and W. M. Griffith, January 1988, Phoenix, AZ.
2. C. M. ADAM and R. G. BOURDEAU, in "Proceedings of the 2nd International Conference on Rapid Solidification Processing: Principles and Technologies II", edited by R. Mehrabian, B. Kear and M. Coehn (Claitor's, Baton Rouge, Los Angeles, 1980) pp. 246–59.
3. W. S. MILLER *et al.*, in "Proceedings of TMS–AIME Symposium on Aluminium Powder Metallurgy", edited by G. J. Hildeman and M. J. N. Koczak, Fall Meeting, Toronto, Canada, 13–17 October 1985, pp. 311–31.
4. G. J. MARSHALL, I. R. HUGUES and W. S. MILLER, *Mater. Sci. Technol.* **2** (1986) 394.
5. E. K. IOANNIDIS and T. SHEPPARD, *J. Mater. Sci.* **25** (1990) 3965.
6. G. CLIFF and G. W. LORIMER, *J. Microsc.* **62** (1975) 246.
7. J. N. PRATT and G. V. RAYNOR, *J. Inst. Metals* **80** (1951–52) 449.
8. R. MANAÏLA, V. FLORESCU, A. JIANU and A. BADESCU, *Phys. Status. Solidi (a)* **109** (1988) 6.
9. *Idem, Philos Mag. B* **60** (1989) 589.
10. D. W. LAWTHER, R. A. DUNLAP, D. J. LLOYD and M .E. McHENRY, *J. Mater. Sci.* **24** (1989) 3076.
11. D. W. LAWTHER, R. A. DUNLAP and V. SRIVINAS, *Can. J. Phys.* **67** (1989) 463.
12. T. OHNISHI, Y. NAKATANI and K. OKABAYASHI, *Bull. Univ. Osaka Pref. Ser. A* **24** (1975) 1.
13. L. K. WALFORD, *Acta Crystallogr.* **18** (1965) 287.
14. JCPDS Tables (1979).
15. P. J. BLACK, *Acta Crystallogr.* **8** (1955) 43.
16. K. F. KOBAYASHI, N. TACHIBANA, P. H. SHINGU, *J. Mater. Sci.* **24** (1989) 2437.
17. H. E. KISSINGER, *Anal. Chem.* **29** (1957) 1702.
18. W. B. ALEXANDER, L. M. SLIFKIN, *Phys. Rev.* **B1** (1970) 3274.

19. I. A. SZABO, D. L. BEKE, F. J. KEDVES, *Key Eng. Mater.* **44–45** (1990) 87.
20. D. BERGNER, *Neue Hütte* **29** (1984) 207.
21. J. PHILIBERT, "Diffusion et transport de matière dans les solides" (Editions de Physique, 1990) p. 107.
22. LAMBOLT and BÖMSTEN, *Neue Hütte* **26** (1972) 52.
23. A. INOUE, H. KIMURA and T. MASUMOTO, *J. Mater. Sci.* **22** (1987) 1758.
24. K. KIMURA, T. HASHIMOTO, K. SUZUKI, K. NAGAYAMA, H. INO and S. TAKEUCHI, *J. Phys. Soc. Jpn.* **55** (1986) 534.
25. J. P. MORNIROLI, *STEEDS Ultramicrosc.* **45** (1992) 219.
26. M. HANSEN (ed.) "Constitution of Binary Alloys" (McGraw-Hill, 1958) p. 94.
27. L. F. MONDOLO, "Aluminium alloys, Structure and Properties" (Butterworths, 1979) p. 284.

Received 8 November 1993
and accepted 14 November 1994